European volcanological supersite in Iceland: a monitoring system and network for the future

Report

D7.5- Grain-size distribution analysis from the tephra fallout instrument system in real-time

Work Package:	*Determination and evolution of eruption source parameters*
Work Package number:	*WP7*
Deliverable:	*Grain-size distribution analysis from the tephra fallout instrument system in real-time*
Deliverable number:	*D7.5*
Type of Activity:	*RTD*
Responsible activity leader:	*Magnus Gudmundsson*
Responsible participant:	*ITEM*
Authors:	*Costanza Bonadonna (UNIGE), Dario Delle Donne (ITEM), Ármann Hoskuldsson (UI) Emanuele Marchetti (ITEM), Laura Pioli (UNIGE), Marco Pistolesi (UNIFI).*

Type of Deliverable:	*Report* *Prototype*	*[X]* *[ ]*	*Demonstrator* *Other*	*[ ]* *[ ]*
Dissemination level:	*Public* *Prog. Participants (FP7)*	*[X]* *[ ]*	*Restricted Designated Group* *Confidential (consortium)*	*[ ]* *[ ]*

Seventh Framework Programme
EC project number: 308377

Index

Abstract

This report describes the procedure proposed to evaluate in real time the total grain size distribution of the tephra fall-out during volcanic eruptions. This is based on real time measurements at selected sites by using the AshSizer, an instrument specifically designed and developed in the framework of the FUTUREVOLC project. Real-time measurements by each single instrument, performed in a limited range of particle diameter, need first to be combined to infer the TGSD of the whole deposit for the size categories detectable with the AshSizer (i.e. -2 to 3.5 phi) and, second, to be analysed in order to extrapolate the complete whole deposit TGSD (i.e. accounting also for the size categories outside the instrument detection limits).

1. Introduction

The total grain-size distribution (TGSD) of particles injected into the atmosphere during volcanic explosive eruptions is crucial to the description of tephra transport and sedimentation, and it is one of the most difficult parameters to constrain out of all eruption source parameters (ESP) needed for numerical simulations of plume and cloud dispersal (e.g. plume height, mass eruption rate, erupted mass). Due to the difficulty of determining TGSD in real time, real-time forecasting of tephra dispersal is mostly performed taking into account specific meteorological conditions and column height, but generic particle size distributions are typically assumed (e.g. Folch 2012; Mastin et al. 2009). As a result, the development of a strategy for the real-time forecasting of TGSD has fundamental implications on both hazard quantification and risk mitigation.

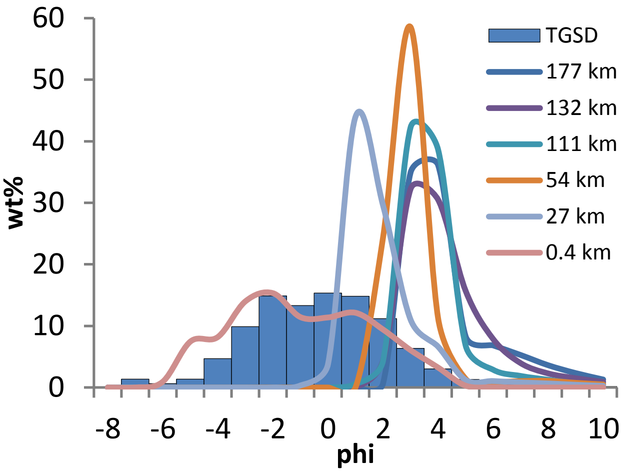

Figure 1: TGSD and single outcrop grain-size distribution of the deposit from the 1996 Ruapehu eruption (New Zealand (Bonadonna et al. 2005b). The numbers in the legend indicate distance from the vent.

TGSD of tephra erupted during explosive eruptions is primarily controlled by magma fragmentation, which is driven by multiple simultaneous processes depending on magma properties (e.g. viscosity, porosity and permeability), and flow-controlled parameters, such as shearing and gas expansion rates (Alidibrov and Dingwell, 1996; Papale, 1999). At the moment there is no model capable of predicting the size distribution of pyroclasts formed during an eruption, and TGSD can be derived only by field studies of the associated tephra deposits (e.g. Bonadonna and Houghton 2005 for a review). Measures of the size of sedimenting pyroclasts in

real time represent the ideal methodology for TGSD assessment, because it is not affected by issues associated with deposit erosion, resuspension and contamination with previous or later eruptive phases, which are the main issues in the current strategies (Eychenne et al., 2011). However, due to various technical limitations, no instrument can give information on the total size range of the particle dispersed in the atmosphere and sedimenting at any given location (e.g. satellite sensors, radars, disdrometers) (e.g. Bonadonna et al. 2011).
TGSDs are typically computed from field data by calculating the weighted average of distributions from single outcrops (Figure 1). The grain-size distribution of particles falling at any given distance from the vent is not representative of the TGSD in the plume, because particles fall at progressively longer distances from the vent with decreasing diameter (Figure 1). In simple terms, the transport distance of volcanic particles (i.e., the distance between the vent and the location of particle sedimentation) is mostly a function of column height, wind profile, and particle diameter, shape and density. As an example, based on numerical simulations, it has been shown that the typical sedimentation distances, normalized by column height, range from 0.2 to 1 to 12 for particles of -6, -1, and 3 phi, respectively, for plumes erupted at the latitudes of Icelandic volcanoes, and wind speed at the tropopause around 45 m/s (Costa et al., 2015). The variability of the sedimentation distance for column heights of 6, 17 and 25 km is shown in Figure 2. The results show a relative stability of the normalized distance with column height and suggest that this parameter can be used as a reference for the location of the sampling sizes, which, suggests that, to sample pumices with sizes comprised between -3 and 3.5 phi, should be positioned along the dispersal axis at distances from the vent comprised between 0.8 and 20 times the column height. We note that these values are also a function of the wind intensity and vertical profile and should be taken only as a general indication. For example, in case of strong winds, the reference normalized distances can increase of about 30% (Costa et al., 2015).
The weighted average of grain-size of individual locations is typically performed using the Voronoi Tessellation strategy (Bonadonna and Houghton, 2005) considering deposit mass/area or thickness (e.g. Figure 1). The main assumption is that the analyzed deposit represents the entire population of the pyroclasts entrained within the eruptive plume. The associated accuracy mostly depends on both the number of measuring stations/outcrops and their spatial distribution.

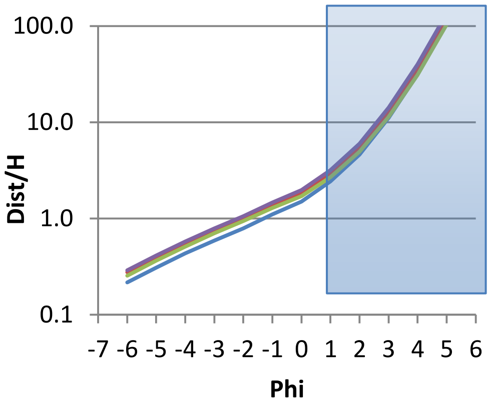

Figure 2: a) Variability of normalized sampling distance of tephra (Dist/H, with Dist= distance and H= column height above vent) with respect to its diameter (in phi). Blue line: column height of 30 km, red line: column height of 10 km; purple line: column height of 17 km; green line: column height of 6 km. The blue area highlights the particle diameter that can be detected by the ash sizer (-2-3.5 phi). Adapted from Costa et al. (2015).

In this report we propose a new strategy to determine the TGSD of tephra deposits in real time based on the use of new laser sensors (AshSizer) developed as a collaboration between ITEM, UNIGE and University of Iceland in the framework of the project FUTUREVOLC (refer to Deliverable 7.3 “Tephra detector, infrasound and cameras” for the technical details of the

sensors). In particular, the AshSizer measures the diameter and fall velocity of particles falling through a laser beam by measuring its obscuration intensity and time and transmit them to a central unit in a real time. It has been designed to work for particles with diameters comprised between -2 and 3.5 phi (i.e. 4 and 0.09 mm). As a result, the new strategy builds on a large dataset of published TGSDs to derive empirical relations that can extrapolate the whole grain-size distribution based on a narrow range of observed size categories (i.e. -2 to 3.5 phi) and on a limited number of instruments (i.e. 10 AshSizer sensors). In addition, we also consider a restriction of access to the area within 10 km from vent, as normally issued during volcanic crisis in Iceland.
In the present report we describe the operation of the AshSizer sensor (section 2), we present the dataset of published TGSDs and describe the empirical relationships developed to constrain the main distribution parameters such as Mdphi and sorting (section 3) and eventually discuss the optimal spatial distribution of AshSizer sensors necessary to construct the TGSD from individual locations (Section 4). Finally, the operational strategy and the associated caveats are presented in section 5.

2. The AshSizer

The AshSizer is a field instrument for real-time automatic measurement of grain-size–distribution of fallout material (Figure 3) developed in the framework of the FUTUREVOLC project by Item s.r.l., in collaboration with University of Geneve, University of Iceland and University of Firenze. The AshSizer, whose prototype was developed during the first half of the project (MS65), was tested during the FUTUREVOLC exercise in June 2014, and was first presented at the Second FUTUREVOLC meeting in September 2014. During the second half of the project 7 AshSizer units were produced and are now available for real-time operation in Iceland during volcanic crises (MS75). The instrument consist into a central unit and an optical barrier (Figure 3). Instrument design and operation is described in detail in D7.3.

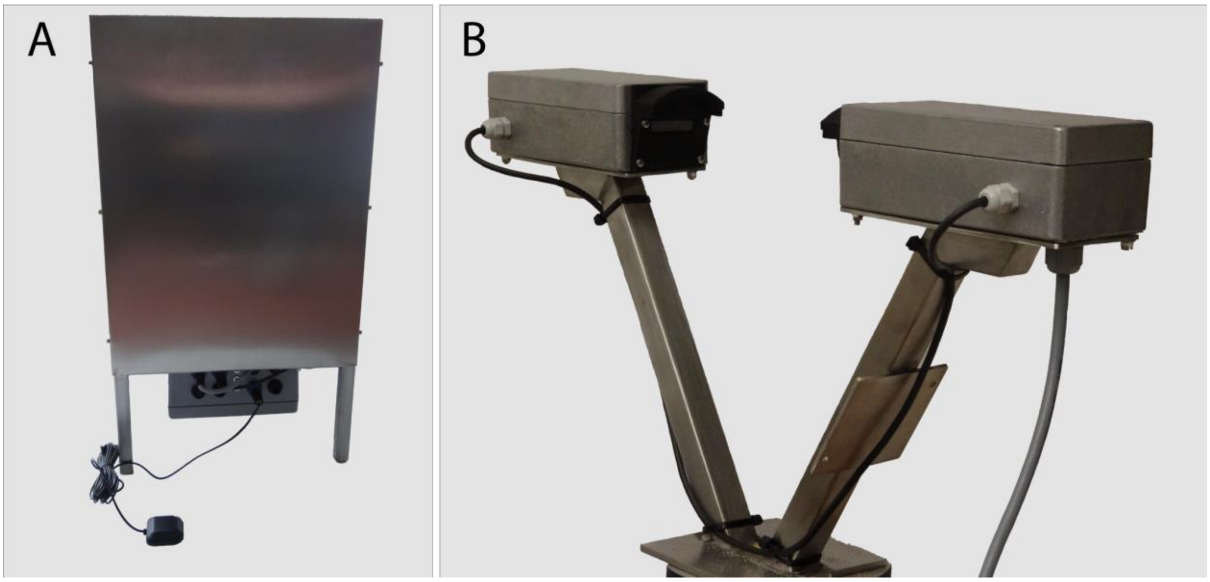

Figure 3: Picture of the AshSizer delivered in Iceland for real-time monitoring of tephra fall-out during explosive volcanic eruptions. The AshSizer consists into a main unit (A) with the electronic board and automatic collector for real-time measurement of accumulation rate and an optical barrier (B), which is used to evaluate in real-time grain size distribution of falling particles and terminal velocity.

The instrument detects particles falling to the ground while crossing a linear laser beam and measures the particle size and terminal velocity from the amplitude and duration of absorption peaks produces by obscuration of the laser beam by the particle as detected by a photodiode. Thikness of the lase beam (1 mm) and sampling rate (30 kHz) were chosen to detect particles in the range of phi spanning between 3.5 and .2 and terminal velocities up to 10 m/s. raw data collected by the instrument are processed in real time locally and particle number density is provided as a function of phi and terminal velocity. Moreover, measurement of the weight and level of the ash accumulating within the collector is performed in real time.
AshSizer is designed to produce one measurement every 30 seconds. Each measurement is stored in the internal memory and is also real-time broadcasted over the internet. Data can be visualized using a stand-alone application developed by Item s.r.l. with the instrument (AshViewer). A web-console is also implemented to check if the AshSizer is properly working, to download the data, and to set the network configuration.
Data from a whole network of AshSizer instruments can be integrated to evaluate the GSD of fall-out material. In order to do that it is required to know exactly how to integrated data from the different sensors and how to extrapolate the measurement outside the limits of sensor operation.

2.1. The AshSizer web console

AshSizer web-console is hosted locally (Figure 4: AshSizer web-console, showing last acquisition data, the GPS status, and allowing to download data and change network settings.). The web page shows the raw output results of the last acquisition (top left) and the current GPS status (top right). The system can be checked that is properly running if the raw output results are refreshed every 30 seconds. Raw output data format will be detailed in the following section. To control the instrument time drift and to detect the instrument position, AshSizer is equipped with on-board GPS allowing us to control the correct time stamp of each measurement. From web console it is possible to check if the system time is correctly set when SHM voice is flagged with a cross (+) or a star (*).
Web console allows also to download the stored data in the internal memory, which consist both on processed and raw data and it also allows to change the AshSizer network configuration (IP address, Netmask, Gateway, and DNS server).

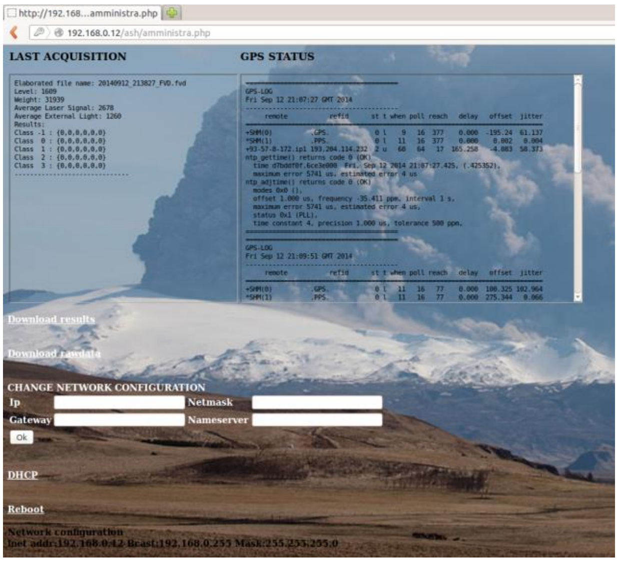

Figure 4: AshSizer web-console, showing last acquisition data, the GPS status, and allowing to download data and change network settings.

2.2. AshViewer

AshViewer is a stand-alone application developed in MATLAB and PYTHON environments and designed for display both real-time data stream (real-time mode) and data files downloaded from the AshSizer (offline mode). Using real time mode AshViewer acquires real-time data from the internet and saves them into the local hard drive. Real time mode is thus designed for monitoring application in case the user needs to have an automatic real time information update of ash fall-out. Using offline mode, the user can display and browse past data downloaded directly from the station. In both modes, AshViewer displays data into main two graphic windows (Figure 5, Figure 6): the statistic window and the time window. The Statistic window shows the grain size and terminal velocity distributions within a time span (usually 15 minutes) that can be set by the operator. This allows a fast visualization of the current characteristics of ash fall out. On page bottom last cumulative ash weight and level from ash collector is also shown. On bottom right some data information are displayed such as the time interval of analysis, the GPS position of instrument, and the last measured thickness and weight from the ash collector.

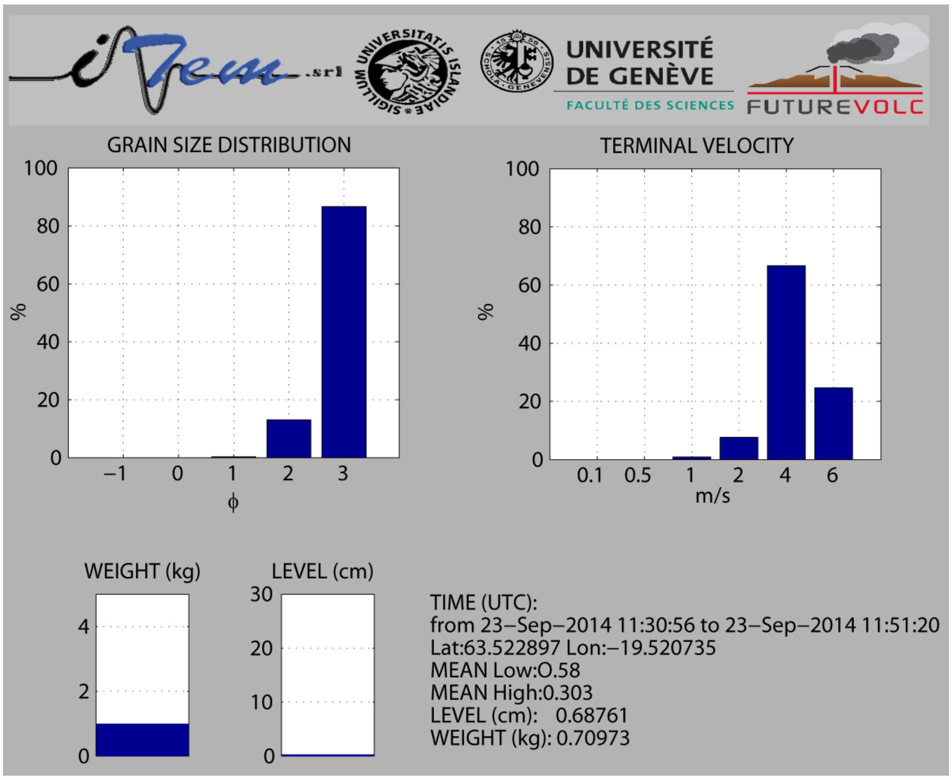

Figure 5: AshViewer statistic window showing real time grain size and terminal velocity distributions, weight and thickness of ash collector.

Real time window shows the results from every single 30 seconds of acquisition in terms of grain size distribution and terminal velocity distribution of the particles, and every weight and thickness measurements from ash collector, within the time span of analysis. This visualization allows to follow evolution through time of the intensity and parameters of ash fall-out and thus is useful for monitoring operations. Ash grain size and terminal velocity relative distributions are displayed using false colours (from white, indicating 0%, to purple, indicating distribution peaks).

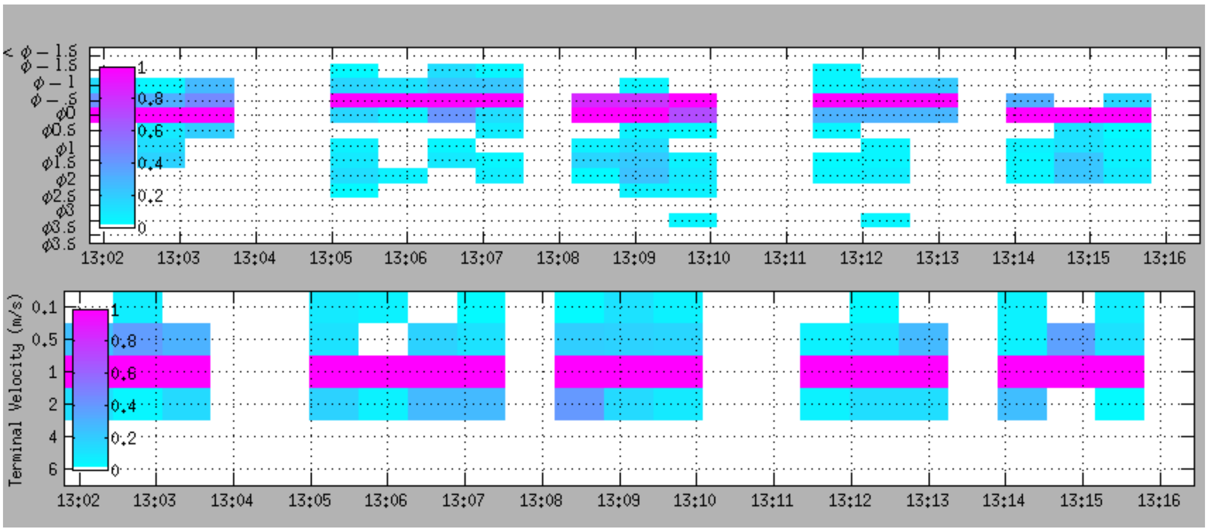

Figure 6: AshSizer real-time window showing ash grain size distribution and terminal velocity distribution associated with every single measurements. This allows to follow evolution through time of the intensity and parameters of ash fall-out.

3. Significance and characteristics of known TGSDs

The amount of observations of tephra deposits considerably increased during the last decade and grain-size distributions from eruptions of different styles (Hawaiian to Strombolian, Vulcanian to subplinian and Plinian) are now better characterized (e.g. Bonadonna and Houghton, 2005; Durant et al., 2009). Grain-size data from 41 eruptions, available from published data (see specific reference list in table 1), encompassing a wide range of eruptive styles, intensities and magma compositions (Figure 8), have been analyzed and compared to find common properties and empirical correlations.

As already mentioned above, the representativeness of each available dataset depends not only on the validity of the numerical method of integration of single outcrop data, but also on the number and distribution of sampling points, which is often limited by geographical constraints (as in the case of islands or large urbanized areas), but also on the accuracy of stratigraphic reconstruction/correlation and sampling issues (for example, in the case of very thick or very fine layers).

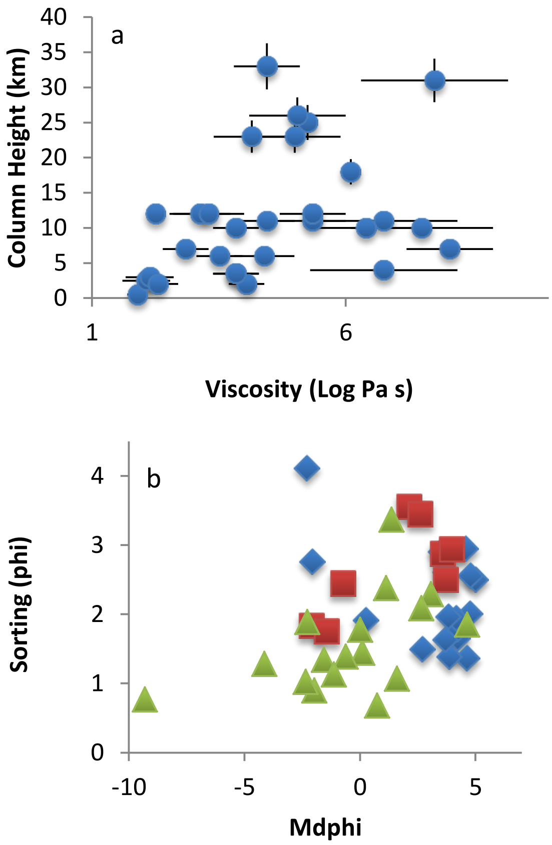

Figure 7: a) Column height (above vent) and magma viscosities of the analyzed eruptions. Viscosities have been calculated taking into account phenocryst content and following the models of Giordano et al. (2008) and Costa et al., (2009); b) Mdphi (i.e. median grainsize, phi_{50}) and sorting (i.e. (phi_{84}- phi_{16})/2) of the TGSDs of the studied eruptions. Red squares: dacite and rhyolite eruptions, blue diamonds: andesite eruptions: green triangles: mafic and alkaline eruptions. See Table 1 for associated references.

3.1. Numerical description of TGSDs

TGSDs have been traditionally described as weight percent of phi classes, in analogy with classical sedimentological methods. They have been fitted using log-normal (wt. %), modified Weibull (wt. %) and power-law distributions (converting weights in number of particles; see for example Brown and Wohletz, 1995, Kaminski and Jaupart, 1999 and Costa et al., 2015). Grain-size distributions are described by two main parameters, Mdphi and sorting, assuming a log-normal (i.e. Gaussian in phi) distribution; in the analyzed eruptions (Table 1) these parameters vary from -9 to -5 phi and 0.7 to 4, respectively. This large variability is not associated with an obvious variability in eruptive styles and magma composition (Figure 7). This lack of correlation and wide spreading is due to several factors, suggesting that the distributions do not follow a simple variability trend. In fact, TGSD can result from several fragmentation processes and their interaction, including co-pyroclastic density currents (co-PDC) coexisting with a main sustained plume and non-steady plume dynamics. These conditions can eventually lead to the formation of bimodal distributions, such as the well-documented case of the Mount St Helens 1980 eruption (Carey and Sigurdsson 1982).

Eruption	Bulk rock composition	Height above vent (km)	MER (kg/s)	Reference
Etna 19-24/07/2001	Basalt	2.5	7.4E+3	Scollo et al. 2007
Etna 27/10/2002	Basalt	3.25	3.0E+5	Andronico et al., 2008a
Etna 24/11/2006	Basalt	0.8	5.0E+3	Andronico et al., 2014a
Etna 4-5/09/2007	Basalt	2	5.0E+3	Andronico et al., 2008b
Etna 12-13/01/2011	Basalt	7	2.5E+4	Andronico et al., 2014b
Izu Oshima 1986	Basaltic andesite	12	1.1E+5	Mannen, 2006
Fuego 1974	Basaltic andesite	10	3.0E+6	Rose et al., 2007
Heimaey 1973	Basalt		1.0E+5	Self et al, 1974
Hekla 2000	Basaltic andesite	11	7.2E+7	Biass et al. 2014
Kilauea Iki, 1959	Basalt	0.6	6.3E+5	Parfitt, 1998
Eyjafjallajokull 4-8/05/2010	Andesite-basalt	7	8.0E+4	Bonadonna et al. 2011
St. Vincent 1979	Basaltic andesite	11	6.0E+6	Brazier et al., 1982
Katla 1625	Basalt			Hoskuldsson unpub. data
Katla 1755	Basalt			Hoskuldsson unpub. data
Al Madinah 1256	Basalt	-	-	Kawabata et al., 2015
Ruapehu 1996	Andesite	6	1.5E+5	Bonadonna and Houghton, 2005
Mt Spurr Aug 1992	Andesite	12	1.7E+6	Durant and Rose, 2009
Mt Spurr Sept 1992	Andesite	12	1.8E+6	Durant and Rose, 2009
Soufriere Hills 31/03/1997	Andesite			Bonadonna et al., 2002
Soufriere Hills 12/09/1997	Andesite	4	-	Bonadonna et al., 2002
Soufriere Hills 15/09/1997	Andesite			Bonadonna et al., 2002
Soufriere Hills 21/09/1997	Andesite			Bonadonna et al., 2002
Soufriere Hills 26/09/1997	Andesite	11	3.0E+6	Bonadonna et al., 2002
Soufriere Hills 28/09/1997	Andesite			Bonadonna et al., 2002
Soufriere Hills 01/10/1997	Andesite			Bonadonna et al., 2002
Soufriere Hills 02/10/1997	Andesite			Bonadonna et al., 2002
Soufriere Hills 10/10/1997	Andesite			Bonadonna et al., 2002
Soufriere Hills 18/07/2005	Andesite	10	1.0E+6	Cole et al., 2014
Soufriere Hills 27/07/2005	Andesite	7	1.0E+6	Cole et al., 2014
Mt. St. Helens 18/05/1980	Dacite	20	1.9E+7	Durant et al., 2009
Cordón Caulle 2011 Unit I	Rhyolite	8-12	5.0E+6	Bonadonna et al. 2015
Askja 1875 phase C	Rhyolite	23	1.0E+8	Sparks et al. 1981
Askja 1875 phase D	Rhyolite	26	8.2E+7	Sparks et al. 1981
Vesuvius 1906 L2	K tephrite	12	1.0E+6	Barsotti et al. 2015

Vesuvius 1906 L3	K tephrite	3-4	1.0E+5	Barsotti et al. 2015
Vesuvius 1906 ash	K tephrite	6-7		Barsotti et al. 2015
Pululagua 2450 BP	Dacite	25±5	-	Volentik et al 2010
El Chichon 1982	Trachyandesit e	27		Sigurdsson et al. 1984
Cotopaxi layer 3	Andesite	23	4E+7	Tsumematsu and Bonadonna, 2015
Cotopaxi layer 5	Andesite	26	6E+7	Tsumematsu amd Bonadonna, 2015
Rungwe pumice	Trachyte	30-35	2-5E+8	Fontijin et al. 2011

Table 1. Eruptions considered in this study, magma composition, column height (H), Mass eruption rate (MER) and reference details.

Power-law fitting of the number of particles (or their cumulative frequency) has been proposed by several authors assuming that magmatic fragmentation generates fractal distributions (e.g. Turcotte, 1986, Kaminski and Jaupart, 1999). A power-law fitting requires the calculation of the normalized number of particles in each class given their cumulative weight. The exact calculation of this value requires the knowledge of the shape, density and size distribution within each size class, and cannot be easily generalized. For this reason, the average particle diameter corresponds to the average phi value between each class and its coarser neighbour, and a generic spherical shape is assumed. In this case the normalized number of particles n_{phi} in each class corresponds to:

$$n_{phi} = \frac{N_{phi}}{N_0} = \frac{wt\%_{phi}}{(d/2)^3 \pi \, \rho_{phi} \cdot 100} \qquad 1)$$

where N_{phi} is the real number of particles, N_o is the total number of particles erupted, and d is the average diameter (in m).

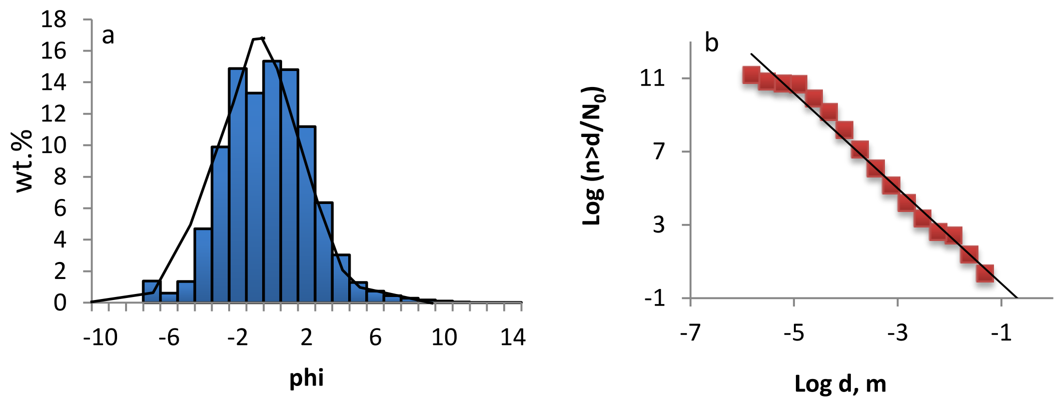

Figure 8: TGSD of the 1996 eruption of Ruapehu 1996 eruption (NZ) fitted with a) log normal and b) cumulative power-law fitting. TGSD data are from Bonadonna and Houghton (2005) (see also Figure 1). d= particle diameter. N_0= total number of particles erupted.

The dependency of pyroclast vesicularity and density on their size has already been shown (e.g. Bonadonna and Phillips 2003, Eychenne et al., 2012). Clast density varies from two-end members, the lowest corresponding to the average vesicularity of lapilli size particles and the largest corresponding to the DRE (dense rock equivalent). The transition from these two values is, with good approximation, linear in phi but the threshold phi sizes are not constant and change within each eruption depending on the original bubble size distribution and density (e.g. Bonadonna and Phillips 2003, Eychenne et al., 2012, Pistolesi et al. 2015). Calculating particle numbers based on a (uncalibrated) fixed density-phi trend would introduce kinks in the distribution leading to non-accurate power-law fitting; for this reason, the assumption of

constant density is more accurate unless specific studies are available for the clast of the TGSD dataset.
The resulting relation will be:

$$\frac{N(z)}{N_0} = \frac{1}{1+\left(\frac{z}{\lambda}\right)^D} \quad 2)$$

with z the class diameter (in m), λ a characteristic length scale and D the power-law coefficient. One example of cumulative distribution of the number of particles is shown in Figure 8b.
In about half of the TGSDs studied, the distribution can be fitted with good accuracy to power-law distributions. In some cases the distribution shows a main power-law trend in the central classes and divergent trend in the fine and/or coarse tail. In any case, even the assumption of a single trend in all the analyzed sizes generates good fitting results with R^2 above 0.98 in about 70% of the cases (Figure 9a). The calculated D ranges from 1.85 to 3.46 with an average value of 2.92. Finally, the values of D calculated over for the complete TGSD were compared with the values of D calculated over the limited size range that can be detected by the AshSizer sensor (-2 to 3.5 phi; Deliverable 7.3). For the sake of simplicity, we have here considered the range -2 to 4 phi. The results show good fitting (in about 66% of cases the two values are not differing of more than 0.5; Figure 9a) except for the TGSDs, that could only be poorly fitted (R^2<0.95) by a power-law distribution. This suggests that narrowing the size range does not significantly affect the estimation of D.

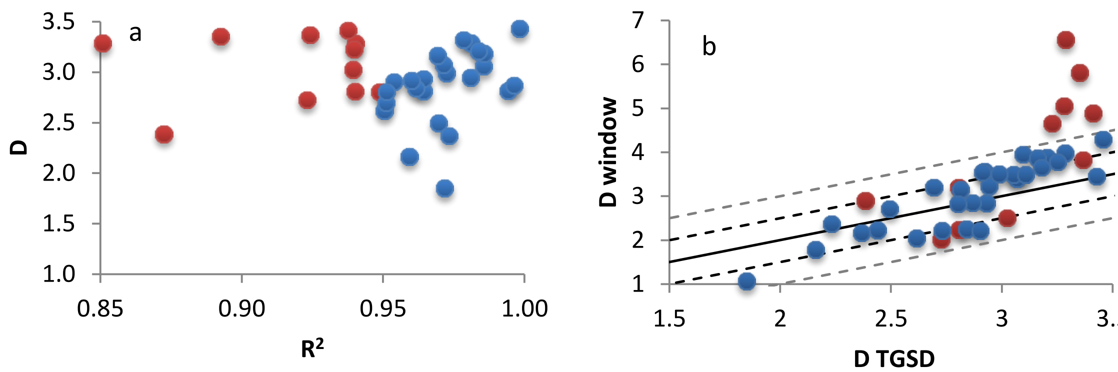

Figure 9: a)Variability of D versus goodness of fit R^2 for fitting of the TGSDs considered in our dataset (Table 1).; b) Comparison between D calculated over the complete TGSD and D calculated over a narrow size range (i.e., -2 to 4 phi). Dashed black and gray lines define a 0.5 phi error and a 1 phi error, respectively. Blue circles represent the data with good fitting (R^2>0.95) that are considered for further analysis. Red circles represent the discarded data due to bad fitting (R^2<0.95).

As mentioned above, the two main parameters used to describe a TGSD are Mdphi and sorting. Below we introduce two emprical correlations for Mdphi and sorting that can be used in real time or when field data are sparse. The coefficient D shows a positive correlation with Mdphi values (Figure 10). This suggests that both parameters are controlled by the fragmentation process and, therefore, they are related. An empirical equation linking D and Mdphi was calculated based on a subset comprising only TGSDs with good power-law fitting (R^2 >0.95, blue circles in Figure 9) and excluding eruptions which had a strong bimodality due to co-PDC components (e.g. eruptions of Mt St Helens 1980 and Soufrière Hills Volcano, Montserrat, 26 September, 1 October and 2 October 1997).

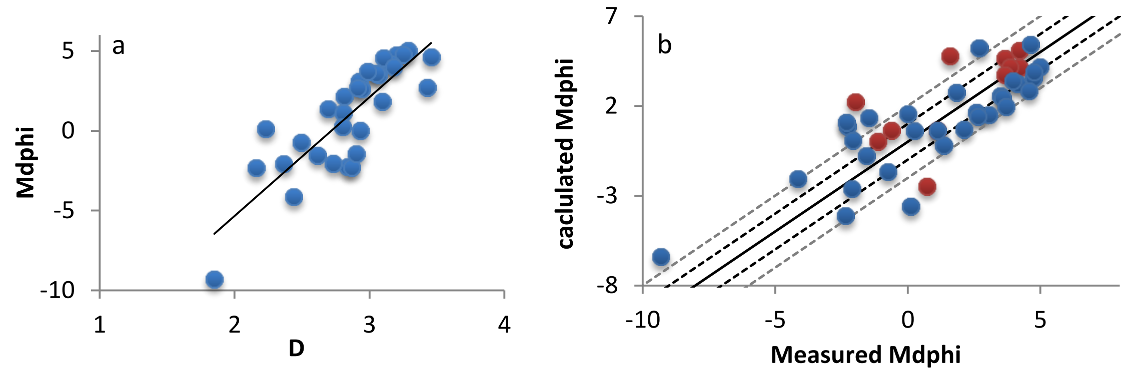

Figure 10: Variability of the best fitting D vs. Mdphi of the selected eruptions (see Figure 9 and main text); b) Comparison between measured and calculated Mdphi: blue circles represent the eruptions used to derive eq. 3); red circles represent the eruptions with bad power-law fitting and, therefore, not used to derive the empirical relation. Dashed black and grey lines define the 1 phi error and 2 phi error, respectively. Note that even the discarded TGSDs (red circles) can be mostly described within a 2 phi error using eq. 3. Symbols as in Figure 9.

The linear relation between D and Mdphi is defined by the trend line (Figure 10a):

$$Mdphi = 7.365\, D - 20.04 \qquad 3)$$

with R^2=0.71 and D comprised between 1.8 and 3.4.
Finally, we note that the sorting of the distributions increases with increasing magma viscosity (η). The relationship is linear, however three main groups of magma viscosity can be identified: low (10^2-$10^{3.5}$ Pa s, i.e. crystal-poor, mafic magmas), intermediate ($10^{3.6}$-10^6 Pa s, i.e. high crystallinity mafic magmas and low cristallinity andesites to dacites) and high (>10^6 Pa s, i.e. mostly associated with dome eruptions) (Figure 11a). Calculations of the fitting parameters have discarded the eruption showing strong bimodality (i.e., Mt St. Helens, Cotopaxi layer 3) for which the calculated sorting is not representative of the distribution. There are only a few examples of the high-viscosity group in the dataset and among them, some TGSDs show strong bimodality and have been discarded. The remaining high-viscosities magma distributions have intermediate sorting values and limited variability (Figure 11a).

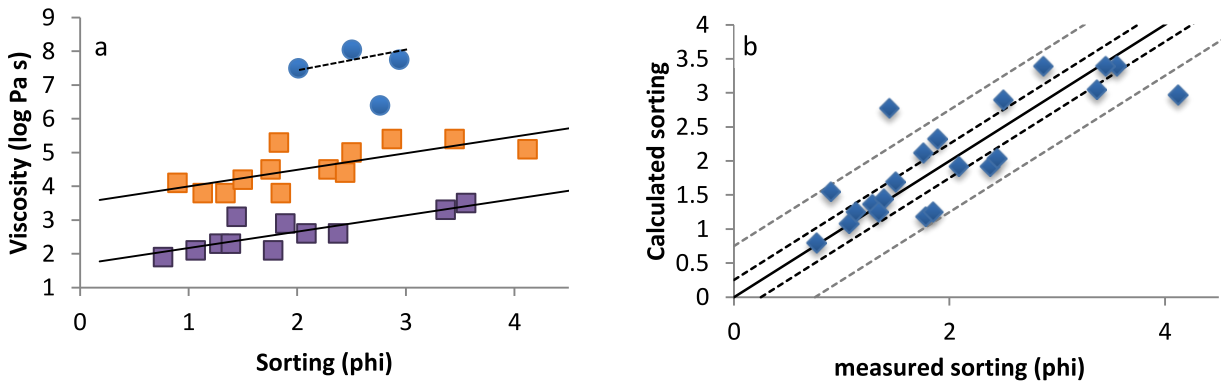

Figure 11: a) Variability of TGSD sorting with the viscosity of the erupted magma. Purple squares: magmas with viscosity comprised between $10^{1.5}$ and $10^{3.5}$ Pa s; Orange squares: magmas with viscosities comprised between $10^{3.55}$ and 10^6 Pa s; blue circles: magmas with viscosities higher than 10^6 Pa s. Eruptions showing strong bimodality have been discarded. b) Comparison between measured and calculated Mdphi for the eruptions used to fit equations 4) and 5). Dashed black and grey lines define the 0.25 phi error and 0.75 phi error, respectively.

The empirical equations for the determination of sorting are:

$$\sigma = 1.382 \log \eta (Pa\ s) - 1.693 \text{ with } R^2\text{=0.68} \qquad 4)$$

for magmas with viscosities comprised between 10^2-$10^{3.5}$ Pa s, and

$$\sigma = 1.419 \log \eta (Pa\ s) - 4.195 \text{ with } R^2=0.69 \quad 5)$$

for magmas with viscosities comprised between $10^{3.5}$-10^6Pa s.

4. Distribution of sampling sites

As explained in the introduction, the non-uniform distribution of particles with different sizes in the tephra blanket has significant implications on the sensitivity of the location of sampling sites for the reconstruction of TGSD. A sensitivity test is necessary to define the best strategy to locate the best sampling array. The test was performed accounting for 10 sampling points (corresponding to 10 AshSizer sensors) and with numerical simulations using TEPHRA2 (Bonadonna et al., 2005a) to generate a synthetic tephra deposit under various eruptive and atmospheric conditions. TGSD was calculated using the Voronoi Tessellation method (Bonadonna and Houghton, 2005) for various sampling array distributions. TEPHRA2 is an advection-diffusion model that describes the solution of the equation of particle diffusion, transport, and sedimentation and can forecast tephra accumulation on the ground relative to a particle-release source (Bonadonna et al., 2005a). Inputs to the model include eruption parameters (e.g. erupted mass, plume height, TGSD), atmospheric parameters (i.e. wind speed and direction at various heights) and grid parameters. Since the AshSizer sensors can only detect a narrow grain-size range, we ran the model with the complete TGSD (-8 to 10 phi) and with a narrow grain-size range (-2 to 4 phi) as input.
The 1996 eruption of Ruapehu volcano (New Zealand) was selected as a case study, mostly because of the exceptional detail of deposit sampling (Bonadonna and Houghton, 2005; Bonadonna et al. 2005b; Cronin et al., 1998; Hurst and Turner, 1999). Simulations include variable wind speeds (10 and 20 m/s) and column heights (10 and 20 km above vent), while, for simplicity, the wind direction was kept constant (i.e. 180° from north, e.g. wind blowing from west to east). We also considered a wind profile typical of mid latitudes and the erupted mass (5.00E+09 kg) as calculated by Bonadonna and Houghton (2005) for the 1996 Ruapehu eruption (Figure 12).

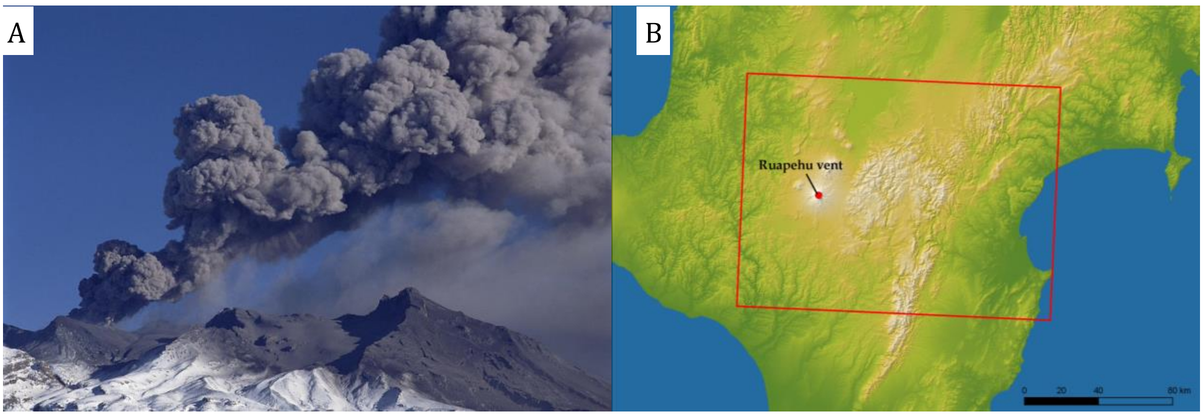

Figure 12: a) The plume associated with the 1996 eruption of Ruapehu (New Zealand). b) The area of interest considered in our sensitivity test.

Outputs of the model include the mass per unit area of tephra on the ground and the wt % of each grain size at the supplied locations. First, we chose an area of interest (Figure 12b) and we used a complete grid of points 1x1 km spaced, 180 km long and 160 km wide (*all_grid*), for a total of 21,000 cells. From the tephra mass load on the ground and the wt. % of each grain size at each grid point (Figure 13 a, b), we assessed the sedimentation of the narrow grain-size range (-2 to 4 phi); the selected locations were positioned within this area.

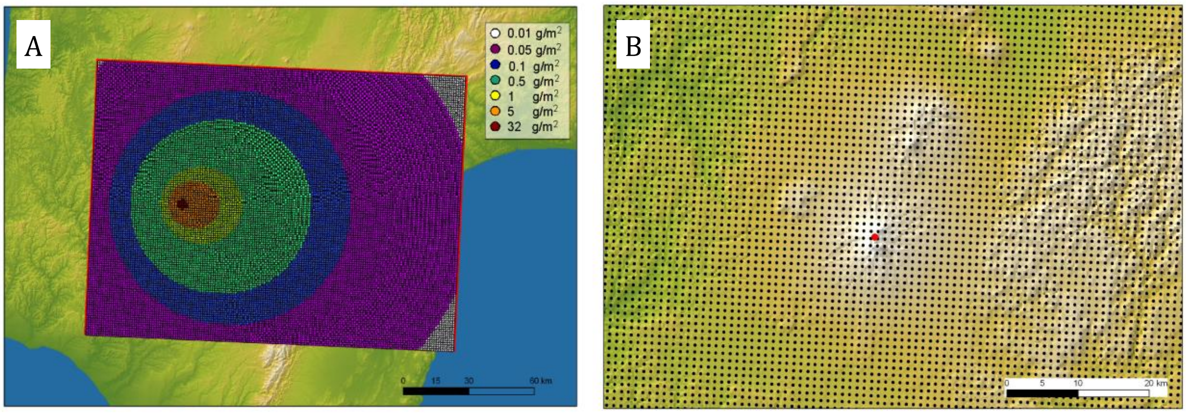

Figure 13: a) Isomass map (g/m^2) for the synthetic tephra deposit for a 20 km high column with a wind speed of 10 m/s and the initial TGSD of Ruapehu 1996 eruption. The red square indicates the extension of the grid considered for the compilation of the synthetic deposit. b) Zoom of the grid around the volcano that shows a selection of the individual grid points.

We ran the model with a grid of 10 points with different geometries, corresponding to the 10 AshSizer sensors to be deployed (Figure 14): 1) 10 points along the dispersal axis equally spaced every 12 km, in order to cover the whole area between 10 km from the vent (beyond the exclusion zone in the case of Icelandic eruptions) and the coastline at 110 km (*DW* geometry; Figure 14a); 2) 10 points chosen at random in the deposition area distributed without any particular alignment and in order to have a 2D configuration which covers most of the area of interest (*random* geometry; Figure 14b); 3) 10 equally spaced points along a crosswind section located at 50 km from the vent (Figure 14c); and 4) 10 points along the dispersal axis spaced at exponential distances from the vent (10, 13, 17, 22, 29, 37, 49, 64, 84, 110 km, Figure 14d and Figure 15).

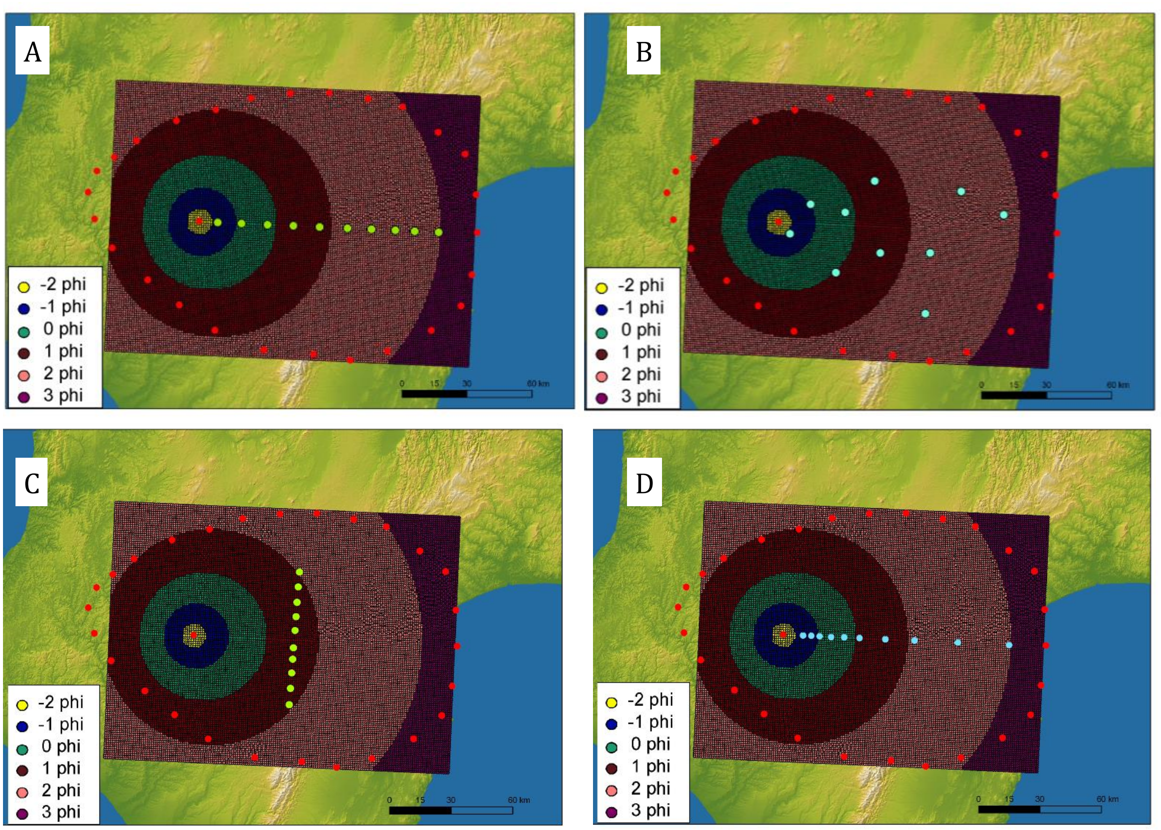

Figure 14: Geometries used for the sensitivity test: a) equally-spaced Downwind (DW) geometry, b) random geometry, c) Cross wind (CW) and d) downwind geometry with exponential increasing of spacing between sampling sites y (DW_exp; see also Figure 15). Red points represent the zero-line used for the Voronoi tessellation.

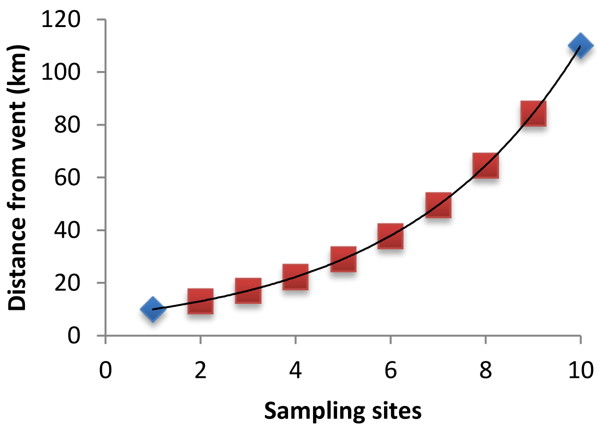

Figure 15: Distribution of sampling points according to an exponentially increasing distance from each other (Figure 14d).

TGSD was calculated by applying the Voronoi tessellation model (Bonadonna and Houghton, 2005) to the 4 geometries of Figure 14. For the Voronoi Tessellation method, each sample is considered as representative of the area enclosed by a polygon centred on the sampling location and contouring the half distance between it and the neighbouring sampling sites (Figure 16). The TGSD is obtained as the area-weighted average of all the Voronoi polygons over the whole deposit. A line of zero deposit also needs to be compiled in order to constrain the area of the external polygons (red points in Figure 14).

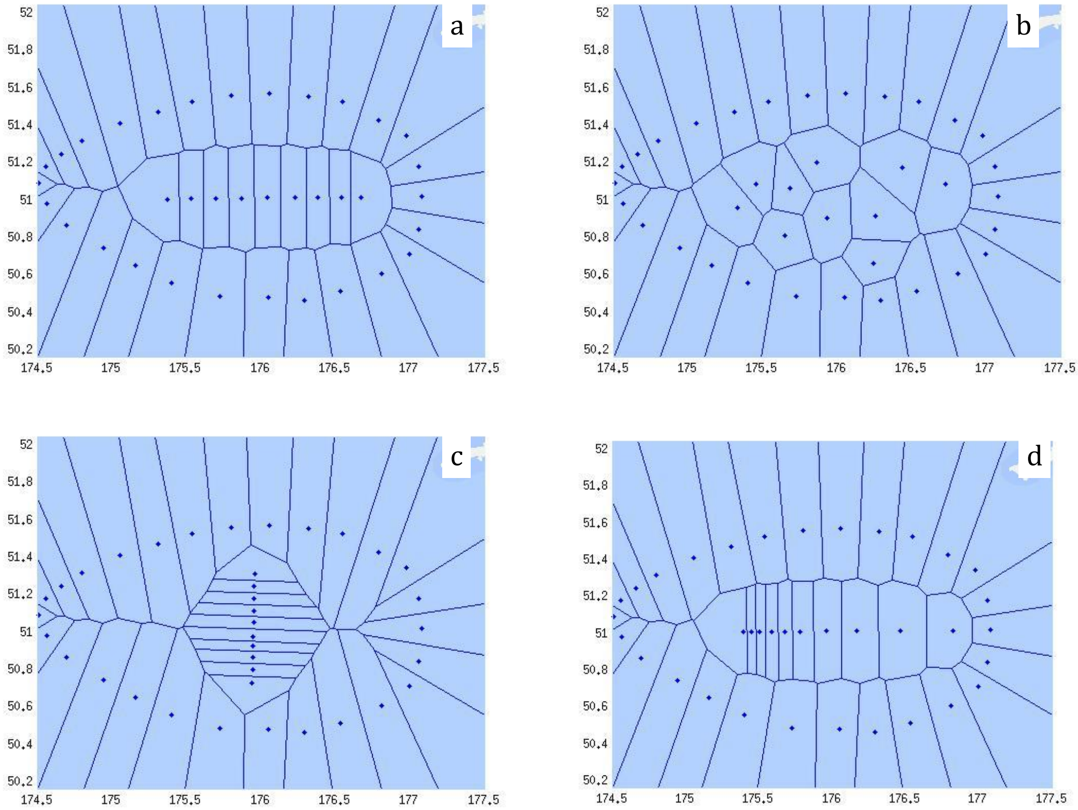

Figure 16: Examples of the Voronoi polygons, for (a) the DW (Figure 14a), (b) random (Figure 14b), (c) CW (Figure 14c), and (d) DW_exp (Figure 14d) distributions.

Because of the wind direction, the deposit and each phi class (-2 to 4 phi) are dispersed towards east, with the coarsest particles (-2 phi) sedimenting close to the volcano. For simplicity, we considered only locations with mass load >0.01 g/m^2, with points with mass load of 0.01 g/m^2 defining the zero line. If we plot the mass for each grain size of interest (-2 to 4 phi), we obtain 7 different areas, with only -2, -1, 0 and 1 phi completely enclosed within the selected grid, and 4 phi completely out (Figure 14). The sedimentation area of 3 phi is already only partly on land. The DW geometry (i.e. equally spaced points in the downwind direction) and the random geometries are representative of all phi categories but 4 phi. CW geometry at 50 km from the vent is fully enclosed within the 1 phi area. The category of -2 phi is not represented in any geometry as it always sediments within 10 km from the vent, typically considered as the restricted zone during volcanic crisis in Iceland.

All the geometries give consistent TGSDs with similar modes and distributions (Figure 17). However, if we consider the complete grain-size range (Figure 17), these are significantly different from the TGSD obtained for the whole deposit as derived by Bonadonna and Houghton (2005), for which the coarser grain-size range is more represented. It is also worth to note that even the TGSD derived from the whole grid (all_grid) is unable to fully represent the real distribution. This discrepancy is mostly due to the restriction of the 10 km distance from vent, which during volcanic crisis in Iceland it would not be accessible.

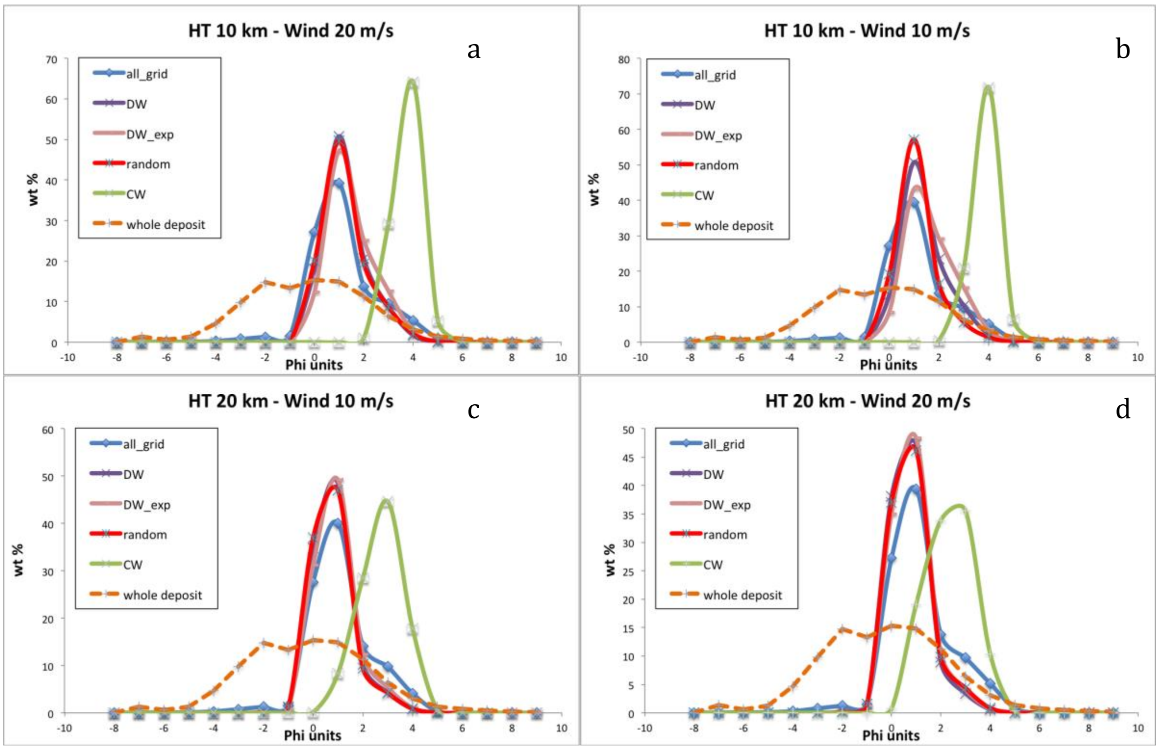

Figure 17: TGSDs obtained with the Voronoi Tessellation for different combination of plume heights and wind speed and associated with: the various sub-sets of the synthetic deposit (Figure 10; DW, DW_exp, random, CW), the whole grid of the synthetic deposit (all_grid) and the whole tephra deposit as determined by Bonadonna and Houghton (2005) (whole deposit).

If we only consider the narrow grain-size range (-2 to 4 phi), we obtain more consistent results (Figure 18), with the TGSD obtained from DW and random geometries being similar to those obtained by using the whole grid, and for different column heights. The CW geometry is unable to reproduce the TGSD, regardless of the grain-size range considered. We conclude that any geometry accounting for the downwind spreading (e.g. DW, DW_exp) is capable of capturing the grain-size features of the whole deposit when a narrow-size range is considered (i.e. -2 to 4 phi). This holds even when the sampling area is restricted (i.e. >10 km from vent).

When considering the range of D calculated from the recovered TSGDs with the different sampling geometries, there is good fitting with any of the simulation of the 20 km high column, Table 2). Among the possible geometries tested in our analysis, the exponential distribution gives a slightly better performance although variations are not significant. The 10 km high column simulations show the worst results with an error on the D estimation up to 1.0. In this case, the minimum sampling distance of 10 km significantly affected the estimation of the coarser grainsize (i.e. -2 phi). This is confirmed by the fact that power-law fitting has a worst performance, with R^2 below 0.88 (Figure 19), and confirms that is essential that the sampling locations are within the falling area of the corresponding narrow grain-size range (-2 to 4 phi), to avoid large error in the estimation of D (and Mdphi). As a result, we conclude that sampling beyond 10 km from vent is able to reproduce the narrow grain-size distribution for the 20 km high column, but could give larger errors in the estimation of D in the case of a 10 km high eruptive column.

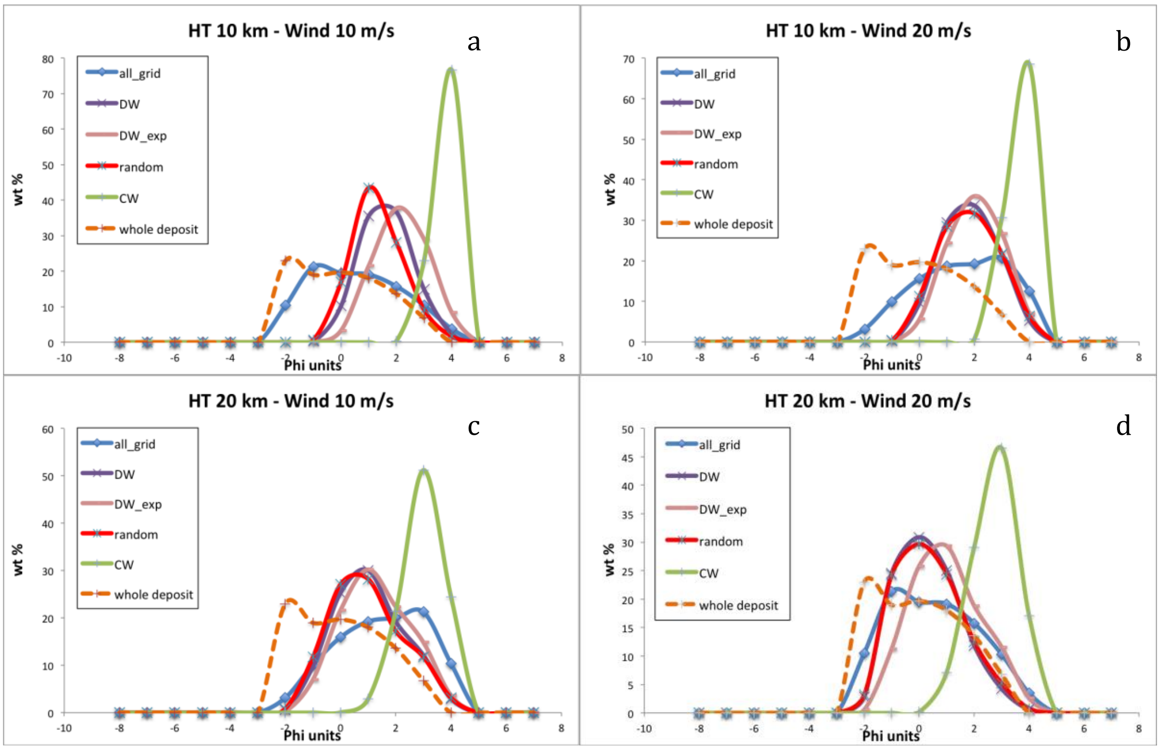

Figure 18: TGSDs obtained with the Voronoi Tessellation for the narrow size range detected by the AshSizer sensor (i.e. -2 to 4 phi) for different combination of plume heights and wind speed and associated with: the various sub-sets of the synthetic deposit (Figure 10; DW, DW_exp, random, CW), the whole grid of the synthetic deposit (all_grid) and the whole tephra deposit as determined by Bonadonna and Houghton (2005) (whole deposit).

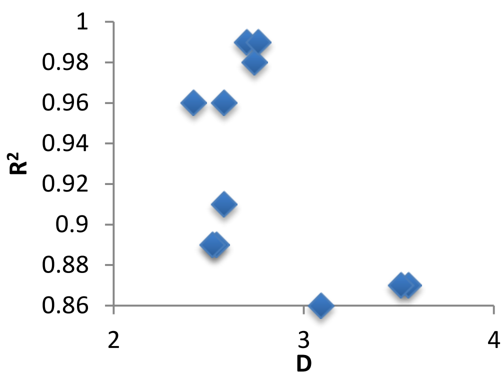

Figure 19: Comparison between D and R^2 of fitting calculated for the initial TGSD and the various recovered distributions. Data from table 2. Note how R^2 increases with D approaching the best-fit value of 2.70. R^2 can be used as a proxy for the validity of D estimation; when below 0.88 D values should be discarded for TGSD estimation because grainsizes are not adequately sampled; high fitting quality suggest that the sampling was adequate.

	Whole deposit TGSD	AshSizer size range	all grid 2020	DW2020	DW2_2020	random 2020	All grid 1010	DW1010	DW_2 1010	Random 1010	Exp_2 020
D	2.58	2.70	2.74	2.54	2.52	2.58	2.76	3.55	3.51	3.09	2.58
R^2	0.97	0.99	0.98	0.89	0.89	0.91	0.99	0.87	0.87	0.86	0.96

Table 2. Results of the power-law fitting of the original Ruapehu TGSD, the THSD associated with the AshSizer narrow size range (-2 to 3 phi), and the various sampling simulations. 2020=20 km column height and 20 m/s wind; 1010 = 10 km column height and 10 m/s wind.

5. Operational strategy

Based on the theoretical strategies and sensitivity tests presented above, we have developed a simple strategy for the reconstruction of TGSD in real time using dedicated AshSizer sensors, which requires:
1) the identification of the best sampling site distribution for the AshSizer sensors based on both eruption dynamics (i.e., column height) and meteorological conditions (i.e. wind intensity and direction);
2) the computation of the relative proportion of the various particle size categories measured at different locations to reconstruct the grain-size distribution of individual locations;
3) the determination of main TGSD parameters (i.e. Mdphi and sorting).
Solving these three fundamental steps requires a complex strategy, which was developed combining theoretical description of grain-size distributions, numerical modelling and empirical observations as shown in the previous sections of this report. The final algorithm is designed to be solved in real time during long-lasting eruptions. Data stability needs to be assessed with time and related to the steadiness of eruptive and meteorological conditions (e.g. plume height, wind intensity and direction). In the following section we describe the procedure to be followed to reconstruct TGSD based on the AshSizer data.
The study in section 3 has shown that an efficient sampling strategy should position the AshSizer sensors along the dispersal axis with increasing spacing distance. In order to compute the total number of particles fallen in the deposit area in the sampling time, the particles counted by each AshSizer need to be combined. A sensitivity test was performed based on the synthetic deposit created with the TEPHRA2 simulations, by calculating a normalized number of particles at each grid point based on the wt. % distribution and mass load. The calculation was carried out with both the Voronoi tessellation method and with a simple sum of the particles counted for each class by each AshSizer. The results show that the results of the two methods are different with the Voronoi method giving results closer to the initial TGSD (narrow size range) (Table 2). As a result, we recommend the use of the Voronoi Tessellation.
In brief, the method proposed consists of 5 main steps (see also Appendix 1 for more detailed instructions):
1) Detection of the grain-size distribution (based on particle number) of a narrow size range (-2 to 4 phi) at each sampling location using an AshSizer sensor (ideally performed at at least 10 sampling locations at distance from the vent between 0.8 to 20 times the column height, along the dispersal axis with exponentially increasing spacing distance between sites).
2) Determination of the TGSD (based on particle number) of the detection narrow size range (-2 to 4 phi) for all AshSizer measurements using the Voronoi Tessellation.
3) Determination of the D of the TGSD of the narrow size range (eq. 2).
4) Determination of the Mdphi of the narrow size range TGSD from the D value calculated above (eq. 3). Such an Mdphi is assumed equivalent to the Mdphi of the whole deposit TGSD (see Figure 9b).
5) Determination of the sorting of the TGSD of the whole deposit based on the magma viscosity (eq. 4 and 5).

5.1. Caveats

The suggested strategy cannot reproduce bimodalities or very complex distributions (i.e. which strongly deviate from a log-normal distribution). These complex distributions could arise from several factors, including:

1) Non uniform sampling (e.g., Tsunematsu and Bonadonna, 2015)
2) Complex eruptive dynamics with multiple fragmentation events which cannot be individually sampled in the deposit (including co-PDC, waxing/waning climactic eruption phases, i.e. Rose and Durant, 2009; Eychenne et al., 2011)
3) Non-uniform magma properties. The role of magma crystallinity in controlling its rheology has been considered in this model; moreover, experimental work of Kueppers et al. (2006) and Perugini and Kueppers (2012) showed that magma porosity controls the overpressure threshold required for fragmentation and the TGSD. Detailed textural analysis of tephra produced during eruptions of different intensities and magmas of different compositions (e.g. Houghton et al., 2004; Gurioli et al., 2005; Lautze and Houghton, 2005) has shown that some magma show non uniform properties up to meso (i.e. cm-) scale and also that they can change during the eruption.
In addition, this strategy is very sensitive to the choice of the sampling sites and particular care should be used when positioning the AshSizer sensors and evaluating their measurements. When the sampling area is limited, either by geographical constrains (i.e. sea, mountains) or by closure of proximal area for security reason, the validity of the AshSizer grain-size detection window to reconstruct TGSD should be verified based on the plot of Figure 2. For example, when sampling is limited to distances of 100 km from the vent, for columns of 15 km or higher, the falling areas of particles of 1 phi or smaller cannot be reached. This suggests that these classes should be disregarded for the D calculations.
Finally, the strategy cannot be applied to very viscous magmas (i.e. crystal-rich), as the paucity of data combined with the complexity of the known distributions (and the eruptions dynamics) did not allow for the development of general relationships and correlations for the calculation of sorting (Figure 11).

Appendix 1

PROCEDURE FOR THE RECONSTRUCTION OF THE TGSD OF A TEPHRA DEPOSIT IN REAL TIME

i) Identification of the best sampling locations for the AshSizer sensors

This step requires knowledge of the wind direction and column height.

Exclusion zone permitting, the AshSizers should be positioned along the dispersal axis at distances from the vent comprised between 1 and 20 times the column height. The sampling sites should have exponentially increasing spacing.

ii) Measurement of the number of particles falling at single locations by their diameters using the AshSizer

This step requires retrieval of the output of the Ashsizers.

The AshSizer will measure the number of particles falling during a definite time interval. The particles will be grouped in phi classes based on their diameter. From the output file the data should be extracted in the form:

PHI CLASS	N of particles
-2	N_{-2}
-1	N_{-1}
0	N_0
1	N_1
2	N_2
3	N_3

iii) Calculation of the total number of particles recorded in each size class

This step requires calculating the total number of particles fallen in the deposition area.

From the output of ii) a total number of particles fallen in the depositional area should be computed by Voronoi tessellation method (i.e., taking into account the spatial distribution of the data). This will provide a TGSD of the narrow size range detected by the AshSizer.

iv) Calculation of the coefficient of the power-law fitting of the cumulative size distribution (i.e., D)

Compute the cumulative power law distribution of the narrow size range TGSD following equation 2) and calculate the best fitting value of D. The value of R^2 of the fitting should also be evaluated. R^2 of 0.96 or higher are a good indicator of the goodness of the D estimation.

v) Calculation of Mdphi of the TGSD of the whole deposit

Calculate the Mdphi of the TGSD of the whole deposit based on eq. 3), assuming that the D estimated from the narrow range is equivalent to the D of the entire distribution.

vi) Estimation of the magma viscosity

This step requires the estimation of magma composition and crystallinity

In order to apply the proposed method, magma viscosity should be calculated by considering the composition of the glass in the groundmass and applying the Giordano et al. (2008) model, also including the effect of dissolved water. The crystals effect on viscosity should be accounted by applying the model proposed by Costa et al. (2009). A set of viscosities calculated on magmas erupted in various eruptions from Icelandic volcanoes is shown in Appendix 2 for reference.

vii) Calculation of the sorting of the TGSD of the whole deposit

The sorting of the TGSD of the whole deposit can be derived by applying equation 5) or 6) for magma with low and intermediate viscosity, respectively.

vi) Description of the TGSD of the whole deposit.

The calculated values of Mdphi and sorting can be used to model a log normal (i.e. Gaussian) distribution with given mean and standard deviation:

$$f(\mathrm{phi}) = \frac{1}{\sigma\sqrt{2\pi}} \exp\left[-\frac{(\mathrm{phi} - MdPhi)^2}{2\sigma^2}\right]$$

where phi is the particle diameter expressed in phi, and σ is the calculated sorting of the distribution.

Appendix 2

Viscosities of magmas erupted in Icelandic eruptions used in the dataset.

Eruption	Magma composition	Crystal volumetric fraction	Magma viscosity (Log Pa s)
Hekla 2000	basaltic	0.05	3.3±0.7
Heimaey	basaltic	0.21-0.15	4.0 ±0.4
Askja 1875, Phase C	Mixed (basalt/rhyolite)	0.05	4.2±0.7
Askja 1875, Phase D	Mixed (basalt/rhyolite)	0.05	5.1±1.0
Katla 1725	basaltic	0.05	2.6±0.2
Katla 1655	basaltic	0.05	2.6±0.2
Ejafjallajokull	Mixed (basaltic/andesitic)	0.25	3.5±0.5

Table A2.1: Examples of basic petrologic characteristics and viscosity estimation of magma erupted during explosive eruptions in Iceland. The error in viscosity estimation derives from uncertainty in the syn-eruptive dissolved water content of the magma.

References

Alidibirov, M., & Dingwell, D. B. (1996). Magma fragmentation by rapid decompression. *Nature*, *380*(6570), 146–148. http://doi.org/10.1038/380146a0

Andronico, D., Scollo, S., Caruso, S., & Cristaldi, A. (2008). The 2002–03 Etna explosive activity: Tephra dispersal and features of the deposits. *Journal of Geophysical Research*, *113*(B4), B04209. http://doi.org/10.1029/2007JB005126

Andronico, D., Cristaldi, A., & Scollo, S. (2008). The 4–5 September 2007 lava fountain at South-East Crater of Mt Etna, Italy. *Journal of Volcanology and Geothermal Research*, *173*(3), 325–328.

Andronico, D., Scollo, S., Castro, Lo, M. D., Cristaldi, A., Lodato, L., & Taddeucci, J. (2014). Eruption dynamics and tephra dispersal from the 24 November 2006 paroxysm at South-East Crater, Mt Etna, Italy. *Journal of Volcanology and Geothermal Research*, *274*(C), 78–91. http://doi.org/10.1016/j.jvolgeores.2014.01.009

Andronico, D., Scollo, S., Cristaldi, A., & Castro, Lo, M. D. (2014). Representivity of incompletely sampled fall deposits in estimating eruption source parameters: a test using the 12–13 January 2011 lava fountain deposit from Mt. Etna volcano, Italy. *Bulletin of Volcanology*, *76*(10), 861. http://doi.org/10.1007/s00445-014-0861-3

Barsotti, S., Neri, A., Bertagnini, A., Cioni, R., Mulas, M., & Mundula, F. (2015). Dynamics and tephra dispersal of Violent Strombolian eruptions at vesuvius. *Bulletin of Volcanology*, 1–19. http://doi.org/10.1007/s00445-015-0.939-6

Biass, S., Scaini, C., Bonadonna, C., Folch, A., Smith, K., & Hoskuldsson, A. (2014). A multi-scale risk assessment for tephra fallout and airborne concentration from multiple Icelandic volcanoes – Part 1: Hazard assessment. *Natural Hazards and Earth System Science*, *14*(8), 2265–2287. http://doi.org/10.5194/nhess-14-2265-2014-supplement

Bonadonna, C., Cioni, R., Pistolesi, M., & Elissondo, M. (2015). Sedimentation of long-lasting wind-affected volcanic plumes: the example of the 2011 rhyolitic Cordón Caulle eruption, Chile. *Bulletin of Volcanology*, *77*(13).

Bonadonna, C., C.B. Connor, B.F. Houghton, L. Connor, M. Byrne, A. Laing, and T. Hincks (2005a). Probabilistic modeling of tephra dispersion: hazard assessment of a multi-phase eruption at Tarawera, New Zealand, *Journal of Geophysical Research, 110 (B03203)*.

Bonadonna C, Phillips JC, Houghton BF. (2005b) Modeling tephra fall from a Ruapehu weak plume eruption, Journal of Geophysical Research, 110, B08209, doi:10.1029/2004JB003515

Bonadonna, C., Genco, R., Gouhier, M., Pistolesi, M., Cioni, R., Alfano, F., et al. (2011). Tephra sedimentation during the 2010 Eyjafjallajökull eruption (Iceland) from deposit, radar, and satellite observations. *Journal of Geophysical Research*, *116*(B12), B12202. http://doi.org/10.1029/2011JB008462

Bonadonna, C., & Houghton, B. F. (2005). Total grain-size distribution and volume of tephra-fall deposits. *Bulletin of Volcanology*, *67*(5), 441–456. http://doi.org/10.1007/s00445-004-0386-2

Brazier, S., Davis, A. N., Sigurdsson, H., & Sparks, R. S. J. (1982). Fallout and deposition of volcanic ash during the 1979 explosive eruption of the Soufriere of St. Vincent. *Journal of Volcanology and Geothermal Research*, *14*, 335–359.

Brown, W. K., & Wohletz, K. H. (1995). Derivation of the Weibull distribution based on physical principles and its connection to the Rosin–Rammler and lognormal distributions. *Journal of Applied Physics*, *78*(4), 2758–2763.

Costa, A., Caricchi, L., & Bagdassarov, N. (2009). A model for the rheology of particle-bearing suspensions and partially molten rocks. *Geochemistry Geophysics Geosystems*, *10*(3). http://doi.org/10.1029/2008GC002138\

Costa, A., Pioli, L., & Bonadonna, C. (2015) Insights into tephra total grain-size distribution from field data analysis. Submitted to EPSL.

Cronin, S.J., Hedley, M.J., Neall, V.E., Smith, R.G. 1998. Agronomic impact of tephra fallout from the 1995 and 1996 Ruapehu Volcano eruptions, New Zealand. Environ Geol 34:21–30.

Durant, A. J., & Rose, W. I. (2009). Sedimentological constraints on hydrometeor-enhanced particle deposition: 1992 Eruptions of Crater Peak, Alaska. *Journal of Volcanology and Geothermal Research*, *186*(1-2), 40–59. http://doi.org/10.1016/j.jvolgeores.2009.02.004

Eychenne, J., & Pennec, J.-L. (2012). Sigmoidal particle density distribution in a subplinian scoria fall deposit. *Bulletin of Volcanology*, *74*(10), 2243–2249. http://doi.org/10.1007/s00445-012-0671-4

Eychenne, J., Le Pennec, J.-L., Troncoso, L., Gouhier, M., & Nedelec, J.-M. (2011). Causes and consequences of bimodal grain-size distribution of tephra fall deposited during the August 2006 Tungurahua eruption (Ecuador). *Bulletin of Volcanology*, *74*(1), 187–205. http://doi.org/10.1007/s00445-011-0517-5

Fontijn, K., Ernst, G. G. J., Bonadonna, C., Elburg, M. A., Mbede, E., & Jacobs, P. (2011). The ~4-ka Rungwe Pumice (South-Western Tanzania): a wind-still Plinian eruption. *Bulletin of Volcanology*, *73*(9), 1353–1368. http://doi.org/10.1007/s00445-011-0486-8

Gurioli, L., Houghton, B. F., Cashman, K. V., & Cioni, R. (2005). Complex changes in eruption dynamics during the 79 AD eruption of Vesuvius. *Bulletin of Volcanology*, *67*(2), 144–159. http://doi.org/10.1007/s00445-004-0368-4

Houghton, B. (2004). The influence of conduit processes on changes in style of basaltic Plinian eruptions: Tarawera 1886 and Etna 122 BC. *Journal of Volcanology and Geothermal Research*, *137*(1-3), 1–14. http://doi.org/10.1016/j.jvolgeores.2004.05.009

Hurst, A.W., Turner, R., 1999. Performance of the program ASH- FALL for forecasting ashfall during the 1995 and 1996 eruptions of Ruapehu volcano. New Zealand J Geol Geophys 42:615–622.

Kaminski, E., & Jaupart, C. (1999). The size distribution of pyroclasts and the fragmentation sequence in explosive volcanic eruptions. *Journal of Geophysical Research*, *103*(B12), 21.

Kueppers, U., Scheu, B., & Spieler, O. (2006). Fragmentation efficiency of explosive volcanic eruptions: A study of experimentally generated pyroclasts. *Journal of Volcanology and Geothermal Research*.

Lautze, N. C., & Houghton, B. F. (2005). Physical mingling of magma and complex eruption dynamics in the shallow conduit at Stromboli volcano, Italy. *Geology*, *33*(5), 425–428. http://doi.org/10.1130/G21325.1

Mannen, K. (2006). Total grain size distribution of a mafic subplinian tephra, TB-2, from the 1986 Izu-Oshima eruption, Japan: An estimation based on a theoretical model of tephra dispersal. *Journal of Volcanology and Geothermal Research*, *155*(1-2), 1–17.

Papale, P. (1999). Strain-induced magma fragmentation in explosive eruptions. *Nature*, *397-428*, 425–425.

Parfitt, E. A. (1998). A study of clast size distribution, ash deposition and fragmentation in a Hawaiian-style volcanic eruption. *Journal of Volcanology and Geothermal Research*, *84*(197-208), 12.

Perugini, D., & Kueppers, U. (2012). Fractal analysis of experimentally generated pyroclasts: A tool for volcanic hazard assessment. *Acta Geophysica*, *60*(3), 682–696.

Rose, W., & Durant, A. (2009). Fine ash content of explosive eruptions. *Journal of Volcanology and Geothermal Research*, *186*(1-2), 32–39.

Rose, W. I., Self, S., Murrow, P. J., Bonadonna, C., Durant, A. J., & Ernst, G. G. J. (2007). Nature and significance of small volume fall deposits at composite volcanoes: Insights from the October 14, 1974 Fuego eruption, Guatemala. *Bulletin of Volcanology*, 25. http://doi.org/10.1007/s00445-007-0187-5

Rust, A. C., & Cashman, K. V. (2011). Permeability controls on expansion and size distributions of pyroclasts. *Journal of Geophysical Research*, *116*(B11). http://doi.org/10.1029/2011JB008494

Scollo, S., Delcarlo, P., & Coltelli, M. (2007). Tephra fallout of 2001 Etna flank eruption: Analysis of the deposit and plume dispersion. *Journal of Volcanology and Geothermal Research*, *160*(1-2), 147–164. http://doi.org/10.1016/j.jvolgeores.2006.09.007

Self, S., Sparks, R. S. J., Booth, B., & Walker, G. P. L. (2009). The 1973 Heimaey Strombolian Scoria deposit, Iceland. *Geological Magazine*, *111*(06), 539–548. http://doi.org/10.1017/S0016756800041583

Sparks, R. S. J., Wilson, L., & Sigurdsson, H. (1981). The pyroclastic deposit of the 1875 eruption of Askja, Iceland. *Philosophical Transactions of the Royal Society of London. Series A*, *299*(1447), 38.

Tsunematsu, K., & Bonadonna, C. (2015). Grain-size features of two large eruptions from Cotopaxi volcano (Ecuador) and implications for the calculation of the total grain-size distribution. *Bulletin of Volcanology*, *77*(7), 64. http://doi.org/10.1007/s00445-015-0949-4

Volentik, A. C. M., Bonadonna, C., Connor, C. B., Connor, L. J., & Rosi, M. (2010). Modeling tephra dispersal in absence of wind: insights from the climactic phase of the 2450 BP Plinian eruption of Pululagua volcano (Ecuador). *Journal of Volcanology and Geothermal Research*, 1–62. http://doi.org/10.1016/j.jvolgeores.2010.03.011